CORE
Metadata, citation and similar papers at core.ac.uk
Provided by NERC Open Research Archive

JOURNAL OF GEOPHYSICAL RESEARCH, VOL. 115, C10051, doi:10.1029/2009JC005797, 2010

Convective heat transfer over thin ice covered coastal polynyas

E. K. Fiedler,[1,2] T. A. Lachlan-Cope,[3] I. A. Renfrew,[1] and J. C. King[3]

Received 11 September 2009; revised 26 February 2010; accepted 26 May 2010; published 23 October 2010.

[1] Polynyas play an important role in the regional meteorology and oceanography of the high latitudes and in the global ocean circulation. Unique low-level observations of an Antarctic coastal polynya, the Ronne Polynya, were conducted using an instrumented aircraft. At the time of the observations, the polynya was mostly covered with thin ice perforated with holes and was composed of two distinct regimes: an inner region of newly formed and thin ice and an outer region of thicker more consolidated ice. The sensible heat flux over the polynya was ~100 W m^{-2} and decreased with fetch, primarily as a result of the thickening ice cover. The mean sensible heat transfer and drag coefficients over the polynya were $C_{HN10} = (0.7 \pm 0.1) \times 10^{-3}$ and $C_{DN10} = (1.1 \pm 0.2) \times 10^{-3}$, respectively. The heat transfer coefficient is similar to that found over heterogeneous sea ice and is significantly lower than has been used in previous studies of heat fluxes over polynyas, which are often assumed to be open water. The transfer coefficients were not found to be a function of fetch or ice conditions as represented by the surface temperature and albedo. The data were used in an investigation of the output of sensible heat flux, potential temperature, and boundary layer depth from a simple fetch-dependent model. For this case study, surface temperatures and transfer coefficients appropriate to an ice-covered surface were required for an accurate simulation.

Citation: Fiedler, E. K., T. A. Lachlan-Cope, I. A. Renfrew, and J. C. King (2010), Convective heat transfer over thin ice covered coastal polynyas, *J. Geophys. Res.*, *115*, C10051, doi:10.1029/2009JC005797.

1. Introduction

1.1. Background

[2] Coastal polynyas are regions of thin ice or open water in pack ice, caused by the offshore advection of the ice by strong continental winds. If the exposed ocean surface is at freezing point, rapid cooling results in the formation of new ice. This ice is also advected offshore in a continuous process. Coastal polynyas (sometimes also termed wind-driven or "latent heat" polynyas) are sites of significant air–sea-ice interactions. Consequently, they play an important role in both the regional meteorology and oceanography of the high latitudes, as well as globally through their impact on the ocean circulation.

[3] During a cold air outbreak over a coastal polynya, when cold air is advected over relatively warm open water, large ocean-atmosphere temperature and humidity differences result in large sensible and latent heat fluxes. Owing primarily to the change in surface temperature between the coast and the polynya, a convective internal boundary layer (CIBL) forms [*Garratt*, 1990]. Sensible and latent heat flux convergence results in warming and moistening of the near-surface air as it crosses the polynya, leading to a reduction in the surface-air temperature and humidity differences with fetch. Given a constant surface temperature and wind speed, this results in a nonlinear reduction in the surface sensible and latent heat fluxes with fetch [*Andreas and Murphy*, 1986; *Grossman and Betts*, 1990; *Chang and Braham*, 1991; *Brümmer*, 1997; *Renfrew and King*, 2000]. This reduction is on the order of 20% over fetches of tens of kilometers and up to 50% over hundreds of kilometers [*Renfrew et al.*, 2002].

[4] Convective clouds and plumes generated by polynyas have been observed to reach heights of up to 4 km [*Smith et al.*, 1990] and are frequently observed on satellite imagery [*Morales Maqueda et al.*, 2004]. Polynyas therefore have the potential to modify and induce mesoscale atmospheric motion and have an impact on regional climate [*Walter*, 1989; *Kottmeier and Engelbart*, 1992; *Alam and Curry*, 1995; *Pinto et al.*, 1995; *Pinto and Curry*, 1995; *Gallée*, 1997; *Dare and Atkinson*, 1999; *Morales Maqueda et al.*, 2004].

[5] The large ocean-atmosphere heat fluxes and continual rapid offshore removal of ice by the wind result in high wintertime rates of ice production, earning this type of polynya the nickname "ice factory." The ice formation process results in extensive brine rejection, leading to salinification of the water column. Combined with surface cooling, this mechanism leads to large buoyancy losses, the initiation of downward convection and the accumulation of

[1]School of Environmental Sciences, University of East Anglia, Norwich, UK.
[2]Now at Met Office, Exeter, UK.
[3]British Antarctic Survey, Cambridge, UK.

Copyright 2010 by the American Geophysical Union.
0148-0227/10/2009JC005797

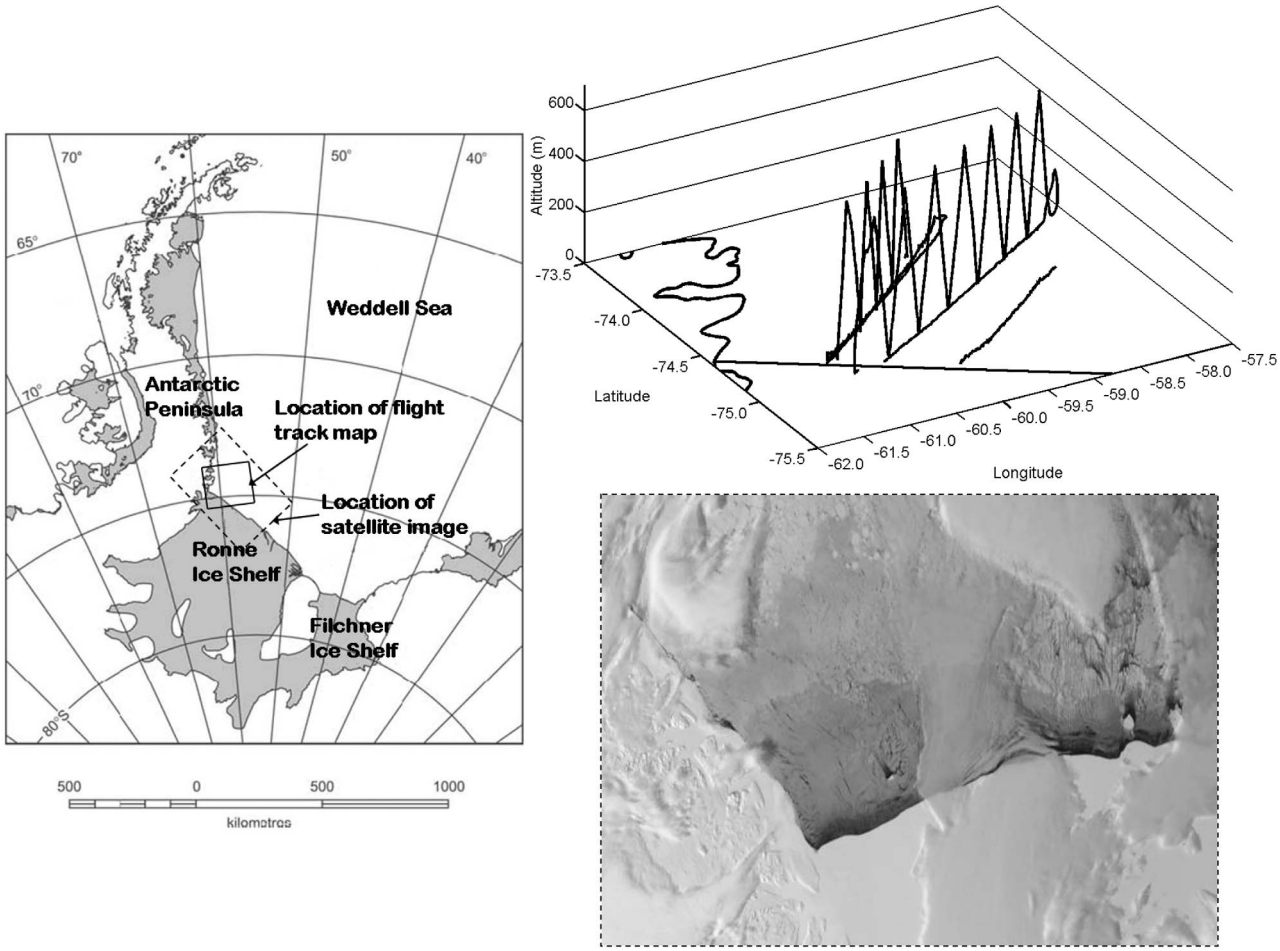

Figure 1. (left) Study region and (top right) flight tracks. F54 flight track is located on left, F57 is center, and F49 is right flight track. The polynya itself can be seen on the gray-scale combined visible and infrared AVHRR image (bottom right) from 28 February 2007 at 1941 UTC, the day of F57. In this AVHRR image, dark colors represent warmer temperatures resulting from low ice concentrations at the polynya. The polynya can also be seen on the AMSR-E image in Figure 4. The locations of both the flight track map and the satellite image are shown on the study region map.

dense water on the continental shelf. This results in the ventilation of deep and bottom water both in the Southern Ocean [*Comiso and Gordon*, 1998] and Arctic Ocean [*Schauer and Fahrbach*, 1999].

[6] Air–sea-ice interactions within coastal polynyas are hence of importance to the local and, consequently, the global ocean circulation. Quantification of the surface energy budget of coastal polynyas is thus an important step toward quantifying ice production and dense water formation rates within them. For this purpose, the ocean-atmosphere sensible heat flux, the largest component of the wintertime surface energy budget [*Markus et al.*, 1998; *Winsor and Björk*, 2000; *Renfrew et al.*, 2002] was investigated at the Ronne Polynya, Antarctica. A combination of aircraft-based observations and modeling was used. The Ronne Polynya is a typical example of a coastal polynya, and hence results obtained from this case study are applicable to the investigation of convective heat transfer over coastal polynyas in general.

1.2. Study Region

[7] The Ronne Polynya is located in the southern Weddell Sea, Antarctica, adjacent to the Ronne Ice Shelf (Figure 1) and is driven by the prevailing offshore winds. The area off the Ronne-Filchner Ice Shelf is one of the most active in the Weddell Sea for coastal polynyas [*Markus et al.*, 1998; *Comiso and Gordon*, 1998; *Renfrew et al.*, 2002]. The approximate mean surface area of the Ronne Polynya is 20×10^3 km^2, but the interseasonal and intraseasonal variability is large. This is thought to be related to variations in atmospheric mesoscale and synoptic features such as storm tracks, cyclones, and barrier-forced winds [*Renfrew et al.*, 2002]. It is a recurring polynya, meaning it opens episodically in the same location, thereby having an important regional impact on the atmosphere and the ocean. The polynya also has an influence on the global ocean circulation through the production of high-salinity shelf water (HSSW), a precursor to Antarctic bottom water (AABW) [*Nicholls et al.*, 2003]. The polynya can be seen in the

Table 1. Flight Information for Low-Level Legs[a]

Flight	Date and Time (UTC)	Mean Altitude (m)	Fetch (km)	$T_{sfc}-T_{air}$ Observed Range (°C)	10 m Wind Speed Observed Range (m s^{-1})	Mean Wind Direction Observed Range (°)
F49L2	25 Feb 2007 1652–1717	32	84.9	2.1–9.0	4.8–6.6	195.9–208.1
F54L1	27 Feb 2007 1518–1543	14	120.9	3.1–12.8	13.3–16.3	204.0–213.5
F54L2	27 Feb 2007 1544–1627	33	127.5	2.9–12.5	8.0–11.5	196.0–208.8
F57L1	28 Feb 2007 1632–1659	15	85.2	4.4–14.0	11.5–12.3	212.5–220.6

[a]F54 and F57 also included a "sawtooth" profiling leg (see Figure 1). Offshore wind direction is assumed to be 180°–225°.

advanced very high resolution radiometer (AVHRR) image in Figure 1.

[8] Using a British Antarctic Survey DHC-6 Twin Otter aircraft, three flights were conducted over the Ronne Polynya. These took place at the end of the austral summer, between 25 and 28 February 2007, during a cold air outbreak off the Ronne Ice Shelf. Flight patterns are shown on Figure 1. In total, four straight and level legs at low altitude and two sawtooth-pattern legs were conducted in the along-wind direction, perpendicular to the front of the Ronne Ice Shelf. Table 1 provides details for the level flight legs, where leg 1 (L1) represents a flight out from the ice shelf and leg 2 (L2) toward it.

[9] Data obtained during these low-level flights are used in this study to provide insights into the variation in surface sensible heat flux with fetch and to obtain new estimates of the sensible heat transfer and drag coefficients over polynyas. Data obtained from aircraft-based profiles through the boundary layer are also presented, illustrating the structure and development of the CIBL formed over a polynya under these conditions.

[10] At the time of the observations, the polynya was mostly covered with thin ice, with no extensive areas of open water. This afforded the opportunity for investigation of heat transfer over thin, heterogeneous sea ice cover. These results are thus applicable not just to studies of polynyas but also to the investigation of regions of similar ice type and concentration, such as within the marginal ice zone (MIZ).

[11] The spatial scale of many smaller coastal polynyas (order 10 km in width) generally lies below the resolution of global (and most regional) ocean-ice-atmosphere models. The recognized impact of polynyas on the regional oceanography and meteorology of the high latitudes and on the global ocean circulation emphasizes the importance of obtaining suitable and accurate parameterizations of the air–sea-ice interaction processes occurring within them. Owing to the current paucity of observational data, the opportunities to validate smaller-scale models, which can provide these parameterizations are limited. Therefore, in this study, the data obtained at the Ronne Polynya were also used to investigate output from a model of the surface sensible heat flux over a polynya during a cold air outbreak, developed by *Renfrew and King* [2000]. The results from this analysis provide insights into the accuracy of the parameters required for successful modeling of the ocean atmosphere heat fluxes and CIBL depth at coastal polynyas.

[12] Only a limited number of comparable aircraft-based observational data sets obtained over leads, polynyas, and sea ice exist [e.g., *Hartmann et al.*, 1994; *Brümmer et al.*, 2002; *Schröder et al.*, 2003; *Walter et al.*, 2006], and all have been obtained in the Arctic. The Antarctic data set presented in this study is therefore unique, owing not only to its Southern Hemisphere location but also to the very low-level (down to 14 m above the surface) extended transects obtained over the heterogeneous ice surface. This has allowed high-quality (i.e., low sampling error) and spatially representative results to be obtained.

[13] The remainder of this paper is structured as follows. Methods are presented in section 2, which includes a description of the aircraft instrumentation and data processing procedures. Methods for the calculation of the surface sensible heat flux and transfer coefficients, as well as quality control of the turbulent flux data are also described. Observations are provided in section 3, beginning with synoptic conditions, surface ice conditions, and boundary layer structure and depth. Results of the investigation into the surface sensible heat flux, transfer coefficients, and their relationships with the surface ice conditions are also provided in this section. In section 4, model estimates of the evolution of the surface sensible heat flux, flight level potential temperature, and CIBL depth with fetch are presented and comparisons with the observational data are made. A discussion and conclusions section follows in section 5.

2. Methods

2.1. Instrumentation and Data Processing

[14] Measurements were made using an instrumented DHC-6 Twin Otter aircraft operated by the British Antarctic Survey. The aircraft was equipped to measure both standard meteorological variables and turbulent fluxes of heat and momentum. Table 2 provides a summary of the instrumentation used and variables measured. Static pressure, dynamic pressure, and total temperature were measured using standard aircraft sensors, while humidity measurements were made using a cooled mirror hygrometer and a Vaisala Humicap sensor. Upwelling and downwelling longwave and shortwave radiation fluxes were measured using Eppley pyranometers and pyrgeometers mounted on the cabin roof and under the belly of the aircraft. The temperature of the surface over which the aircraft was flying was measured using a downward-looking Heitronics KT19.82 infrared thermometer, while a downward-pointing video camera provided a record of surface conditions.

[15] A Best Aircraft Turbulence, or BAT, probe [*Garman et al.*, 2006] was used to obtain measurements of temperature and three-component wind vector at a frequency of 50 Hz, which corresponds to a sampling interval of 1.26 m

Table 2. Aircraft Instrumentation

Variable	Instrument	Sampling Rate	Resolution	Estimated Accuracy
True airspeed, angle of attack, sideslip angle, fast response temperature	NOAA ARL 9 hole BAT (Best Aircraft Turbulence) probe	50 Hz	Airspeed 0.1 m s^{-1}, angles 0.05°, temperature 0.01°C	Airspeed 2%, angles 0.5°, temperature 0.5°C
Static pressure, dynamic pressure	Honeywell HPA sensors	5 Hz	0.1 hPa	0.1 hPa
Total temperature	Rosemount 102E4AL non-deiced, Rosemount 102AU1AG deiced	0.7 Hz	0.01°C	0.3°C
Aircraft attitude, altitude, position, velocity	Javad AT4 4-antenna GPS	20 Hz	Altitude 1e-6 rad, altitude 1e-6 m, position 1e-5 m, velocity 1e-6 m s^{-1}	Altitude: roll/pitch 0.05° and heading 0.03°, altitude 5 m, position 3 m, velocity 0.1 m s^{-1}
Aircraft altitude	Radar altimeter (<800 m above surface)	0.7 Hz	0.25 m	3 m
Dew point	Buck 1011C cooled mirror hygrometer	1 Hz	0.01°C	0.1°C
Relative humidity	Vaisala Humicap HMP45	0.7 Hz	0.1%	3%
Shortwave radiation	Eppley PSP pyranometers	10 Hz	0.5 W m^{-2}	3%
Longwave radiation	Eppley PIR pyrgeometers	10 Hz	1 W m^{-2}	3%
Surface temperature	Heimann KT 19.82 infrared radiation thermometer	10 Hz	0.1°C	1°C
Visual record	Sony DCR-TRV60E DV video (downward) and Sony DCR-HC44E DV video (cockpit), digital handheld camera (cockpit)	25 fps up to 90 min duration, camera as required		

at the aircraft's level flight true airspeed of 63 m s^{-1}. The probe was mounted on the end of a 3 m boom positioned at roof level, which extended along the center line of the aircraft to just forward of the nose. The BAT probe incorporates sensors for dynamic and static pressure, together with differential pressure sensors for computing attack and sideslip angles, and a thermocouple sensor for fast response temperature measurements. All BAT probe sensors were low-pass filtered at 30 Hz and then oversampled at 1600 Hz to avoid aliasing before block averaging to provide data at 50 Hz. Measurements of all three components of aircraft position, attitude, and velocity were provided at a rate of 20 Hz by a JAVAD AT4 four-antenna GPS system. Data from all instruments were recorded using an onboard computer system. GPS time signals from the JAVAD system were used to provide a common time base for all sensors.

[16] Calculations of timeseries of corrected temperatures and all three wind components in an Earth-referenced frame were carried out according to standard procedures [e.g., *Lenschow*, 1986]. Briefly, measurements of true air speed, angle of attack, and sideslip angle from the BAT probe were used to compute wind components relative to the aircraft. Altitude data from the GPS system were then used to rotate these components onto Earth-referenced axes. Finally, the components of aircraft motion output by the GPS system were subtracted to give Earth-referenced wind components. The vertical component of the wind was corrected for the effects of flow distortion around the aircraft using the procedure of *Crawford et al.* [1996]. Optimal calibration coefficients for the BAT probe were determined by flying a series of calibration maneuvers [*Lenschow*, 1986]. Manufacturer-supplied calibrations were used for all other instruments. Downwelling shortwave radiation under clear-sky conditions (appropriate for flights F54 and F57) was corrected for aircraft attitude variations using the procedure of *Bannehr and Glover* [1991]. A small correction was applied for all three flights to the measured upwelling shortwave radiation to account for the fraction of the instrument's field of view obscured by the aircraft undercarriage. A correction was also applied to the surface temperature, assuming the highest measured temperature over the polynya corresponded to open water at the freezing point, i.e., −1.9°C [e.g., *Nicholls et al.*, 2004]. For late summer (or winter) conditions in this region, this is a reasonable assumption.

2.2. Calculation of Turbulent Fluxes

2.2.1. Eddy Covariance Method

[17] The surface sensible heat flux (Q_S) was calculated using the eddy covariance method [*Busch*, 1973], where

$$Q_S = \rho c_p \overline{w'T'}, \tag{1}$$

ρ is the air density, c_p is the specific heat capacity of air, and w' and T' are the vertical wind speed and temperature perturbations, respectively, from the mean over the averaging period or run. The bar denotes the mean value of the covariance over the run.

[18] The momentum flux or wind stress (τ) is given by

$$\tau = \rho\left(\overline{u'w'}^2 + \overline{v'w'}^2\right)^{1/2} = \rho u_*^2, \tag{2}$$

where u', v' are the along-wind and cross-wind components, respectively, of the horizontal wind. The vector sum of these two stresses gives the total kinematic stress, and u_*, the friction velocity, is the square root of the magnitude of the kinematic stress, i.e., $u_* = (\overline{u'w'}^2 + \overline{v'w'}^2)^{1/4}$.

2.2.2. Bulk Method

[19] If high-frequency data are not available, surface fluxes can be estimated using bulk aerodynamic formulae [e.g., *Hartmann*, 1994]. The bulk sensible heat flux and wind stress are given by

$$Q_S = \rho c_p C_{Hr} U_r (T_{sfc} - \theta_r), \tag{3}$$

$$\tau = \rho C_{Dr} U_r^2. \tag{4}$$

Subscripts sfc and r denote the surface and a reference height, respectively. U is wind speed, T is temperature, and θ is potential temperature. Following boundary layer convention, θ is defined as $T + \Gamma z$, where Γ is the adiabatic lapse rate (9.8×10^{-3}°C m^{-1}) and z is the measurement height in m. C_H and C_D are empirically determined coefficients for sensible heat transfer and drag. Calculation of surface fluxes by this bulk method therefore requires accurate determination of these transfer coefficients appropriate to the particular surface under investigation and the atmospheric stability.

[20] Using equations (1) and (2) together with equations (3) and (4) yields equations (5) and (6), into which observations can be substituted to determine values for these coefficients at the measurement or reference height (r),

$$C_{Hr} = \frac{\overline{w'T'}}{U_r(T_{sfc} - \theta_r)}, \tag{5}$$

$$C_{Dr} = \frac{\left(\overline{u'w'}^2 + \overline{v'w'}^2\right)^{1/2}}{U_r^2}. \tag{6}$$

In order to compare measurements made under different stratification conditions and at different measurement heights, values of the bulk coefficients C_{Dr} and C_{Hr} can be converted to equivalent neutral stability values reduced to a reference height of 10 m, i.e., C_{DN10} and C_{HN10}.

[21] Following *Andreas and Cash* [1999],

$$C_{DN10} = \frac{C_{Dr}}{\left\{1 - \kappa^{-1} C_{Dr}^{1/2} [\ln(r/10) - \Psi_m(r/L)]\right\}^2}, \tag{7}$$

$$C_{HN10} = \frac{C_{Hr}}{\left(\frac{C_{Dr}}{C_{DN10}}\right)^{1/2} - \kappa^{-1} C_{Hr} C_{DN10}^{-1/2} [\ln(r/10) - \Psi_h(r/L)]}, \tag{8}$$

where κ is von Karman's constant (0.4) and Ψ_m and Ψ_h are nondimensional stability functions. The ratio r/L or ζ is the stability parameter, where L is the Obukhov length. Following *Andreas and Cash* [1999], the following parameterizations for $\Psi_m(\zeta)$ and $\Psi_h(\zeta)$, appropriate for the unstable stratification conditions of the Ronne Polynya surface layer ($\zeta < 0$), were used [*Paulson*, 1970],

$$\Psi_m(\zeta) = 2\ln[(1+x)/2] + \ln[(1+x^2)/2] - 2\tan^{-1} x + \pi/2,$$

$$\Psi_h(\zeta) = 2\ln\left[\left(1+x^2\right)/2\right],$$

where $x = (1 - 16\zeta)^{1/4}$.

2.3. Flux Data Quality Control

[22] Choosing the length of the averaging period for the eddy covariance calculations is a balance between retaining a high spatial resolution but obtaining statistically significant fluxes. An averaging interval or run of 8.8 km was chosen, which corresponds to an averaging period of 140 s at the aircraft level flight true airspeed of 63 m s^{-1}.

[23] The reliability of the data and the adequacy of the chosen averaging interval were investigated. The methods used for this quality control included examination of the power spectra for individual flux components, the cumulative summation of the covariances and the cospectra and ogives [e.g., *Friehe et al.*, 1991; *French et al.*, 2007]. This was undertaken for each of the sensible heat and momentum flux runs of 8.8 km for the four low-level legs. Figure 2 provides examples for the sensible heat flux of reliable ("good") runs and unreliable ("bad") runs, which were rejected. Similar results were found for the momentum flux.

[24] The example power spectra for temperature perturbations (Figure 2a) illustrate that the energy decreases along the expected −5/3 gradient of the inertial subrange. This indicates the response of the sensors was sufficiently fast to capture all the turbulent wavelengths. The example unreliable or "bad," run (Figure 2a, right) shows a substantial dip in the T' spectrum within the energy-containing range. The dip in the spectrum is not present for the "good" run (Figure 2a, left). This demonstrates why the spectra for the "bad" run (F54L2R14) are also "bad" (Figures 2b–2d, right). The poor data may either be due to measurement errors resulting from instrument problems or because conditions do not meet the strict criteria for Reynolds averaging to be meaningful, i.e., conditions are not homogeneous and stationary.

[25] Figure 2b shows linear cumulative summations for the sensible heat flux. For these plots, a constant gradient for the entire run is desirable, as this demonstrates horizontal homogeneity of the flux with distance. Large deviations from the 1:1 line indicate the presence of coherent disturbances in the flow. For some runs, this inhomogeneity affected the total energy by up to 40% over a small proportion of the run fetch (e.g., Figure 2b, right) and was therefore a basis for rejection of the run.

[26] The cospectra for the fluxes were also examined (Figure 2c). This ensured all flux-carrying wavelengths were included within the averaging period and confirmed all the measured flux was present within the expected turbulent wavelengths of 50 m to 3 km [*Stull*, 1988] and not derived from the larger scale, e.g., synoptic disturbances. It can be seen on Figure 2c (right) that there is power at relatively long wavelengths (low wavenumbers) for the "bad" runs. The ogives (cumulative summation of the covariance, Figure 2d) should ideally resemble a smooth S shape. The asymptotic values at both high and low frequencies (high and low wavenumbers) indicate where there is no contribution to the power in comparison with the other frequencies and demonstrate the wavelengths within which the flux in the cospectrum is contained. Again, the difference between "good" and "bad" runs is clear from Figure 2d. Disturbances which appear in the "bad" cumulative summation plots (Figure 2b, right) are often also apparent on the

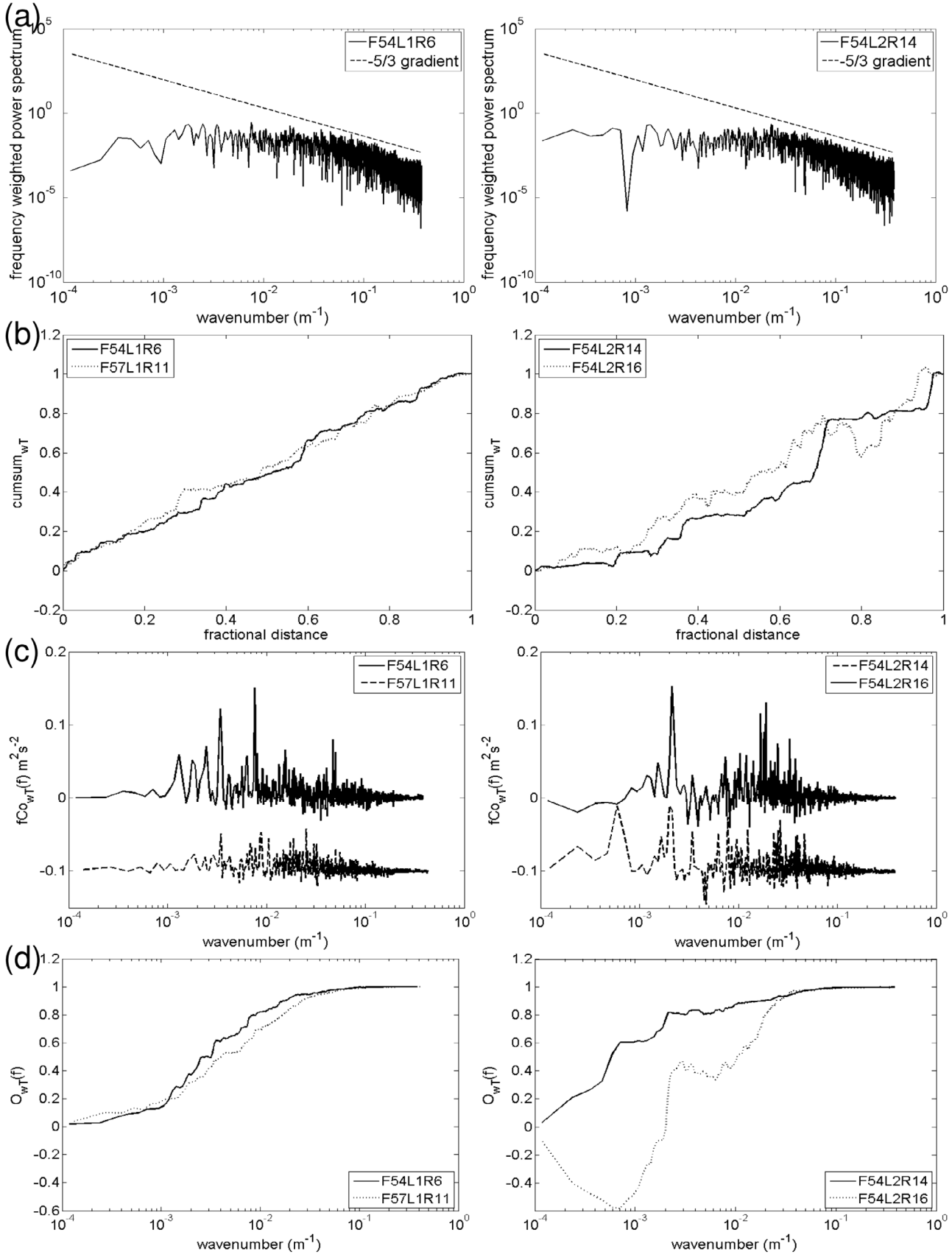
(a)
F54L1R6
-5/3 gradient
F54L2R14
-5/3 gradient
frequency weighted power spectrum
wavenumber (m-1)
(b)
F54L1R6
F57L1R11
F54L2R14
F54L2R16
cumsum wT
fractional distance
(c)
F54L1R6
F57L1R11
F54L2R14
F54L2R16
fCo wT(f) m2s-2
wavenumber (m-1)
(d)
O wT(f)
F54L1R6
F57L1R11
F54L2R14
F54L2R16
wavenumber (m-1)

Figure 2

correspondingly "bad" cospectra and ogives (Figures 2c and 2d, right).

[27] Seven heat flux runs out of a total of 49 (14%) were discarded on the basis of the above analysis. Seven momentum flux runs were also discarded, although these were not all the same as the discarded heat flux runs. As a comparison, based on a similar analysis of turbulence data collected from an aircraft platform, 17% of sensible heat flux runs and 8% of momentum flux runs were discarded by *Petersen and Renfrew* [2009]. For both of the two lowest altitude legs in this study (see section 1.2), no runs were rejected on the basis of the spectral analysis quality control. For these legs, a greater number of eddies were sampled as a result of the lower measurement height, resulting in fluxes with a higher statistical significance. This reduced the scatter or variance in the data, i.e., the "sampling error" (section 3.4.1), increasing the reliability of the data. However, one run from these legs (F54L1R1) was rejected owing to a malfunction in the GPS system, which affected the wind measurements for this single run.

[28] On the basis of the cospectra and ogives analyses, most of the flux for these runs is carried by eddies with wavelengths between about 50 m and 2 km (wavenumbers 2×10^{-2} and 5×10^{-4} m^{-1}). Hence the power is derived from turbulent eddies rather than large-scale disturbances in the flow. This is a consistent characteristic between runs, demonstrating the reliability of the data set and the confidence that can be placed in the results of this study.

[29] The spectral analysis also indicated that the selected averaging interval or run of 8.8 km was appropriate for capturing all of the turbulent flux. The spectra for the accepted runs, particularly those of the lower level legs, are very reliable since this sampling length includes several of the longest wavelengths of the turbulence being measured. Therefore, the averaging interval is long enough that few data points are rejected and the data can be used with confidence in its accuracy, while spatial detail for the investigation into variation of the fluxes with fetch is still retained. According to *Brümmer et al.* [2002], fluxes averaged over longer intervals will follow the more detailed structure of the surface fluxes in a kind of smoothed curve. For this study, the level of spatial detail in the surface fluxes afforded by an 8.8 km sampling length is ideal for comparison to a model output (see section 4). Additionally, this averaging interval compares well with the 8 km sampling length used by *Schröder et al.* [2003], selected after analysis of the random and systematic errors in similar low-level aircraft-based flux data. They also determined that values of their calculated surface transfer coefficients were not dependent on the selected sampling length.

3. Observations

3.1. Synoptic Conditions

[30] A persistent low-pressure system situated in the Weddell Sea induced a cold air outbreak off the Ronne Ice Shelf at the time of the observations. This system produced the steady moderate to strong offshore winds (Table 1) responsible for the opening of the Ronne Polynya at this time. Weather conditions during flight F57 were clear and sunny, while for F54 it was sunny with some high-altitude cloud. For F49 some cumulus cloud was present within the CIBL, but no precipitation was observed.

3.2. Surface Ice Conditions

[31] As mentioned in section 1, at the time of the observations, the Ronne Polynya was mostly covered with thin ice, with no extensive areas of open water. A measured decrease in surface temperature and an increase in albedo with fetch (Figure 6) indicates this ice cover increased in thickness with fetch.

[32] Two regions can be distinguished within a wind-driven polynya, such as the Ronne Polynya. These correspond to an inner region of open water and frazil ice and an outer region of new and young ice floes formed by frazil ice accretion and surrounded by first-year ice [*Morales Maqueda et al.*, 2004]. *Liu et al.* [1997] refer to these regions as the "active polynya" and "young ice" regions, respectively. In this study, both regions are considered to be part of the polynya.

[33] The surface ice cover observed at the Ronne Polynya can be split into two distinct areas or regimes, which correspond to these two regions. They can be clearly identified on Figure 3a, a scatterplot of the surface shortwave albedo and surface temperature, for all points from F54L1 and F54L2. The data have been averaged so that each point has a resolution of 1 km.

[34] The boundary between regimes for F54 shown on Figure 3a is at a fetch of 35 km from the front of the Ronne Ice Shelf. This boundary has been determined subjectively using the gradients of the best fit lines for each regime, i.e., by selecting the division between the points which fitted best to these gradients. Ice conditions at a few points after this boundary are better suited to the first regime, indicating there is not an absolute cutoff point. Using a similar method, the boundary between regimes for F57 was found to be at a fetch of 55 km. A division between regimes for F49 was not apparent. Even by the end of the 90 km leg of this flight, there were still a significant number of areas of open water and thin ice within the more consolidated ice. This can be seen on the plots of surface temperature and albedo with fetch for this leg (Figure 6). Therefore, a distinct second regime, as defined for the other legs, was not present for this case.

[35] For both flights F54 and F57, the r^2 values (coefficient of determination, i.e., how much of the variation in albedo is related to variations in surface temperature) for the albedo-surface temperature trends are higher for the first regime than for the second. For F54, the values are 0.93 and 0.78, while for F57 they are 0.95 and 0.77. The stronger relationship indicates a more uniform ice type within the first regime than within the second. This feature is also

Figure 2. Examples of spectral analysis for (left) good and (right) bad runs of 8.8 km for eddy covariance sensible heat flux. F represents a flight, L for a low-level leg, and R for a run number of 8.8 km within that leg. (a) Power spectra, (b) cumulative summation, normalized by total covariance, (c) frequency-weighted cospectra, where F57L1R11 and F54L2R14 are offset by -0.1 m^2 s^{-2} for clarity, and (d) ogives, normalized by total covariance.

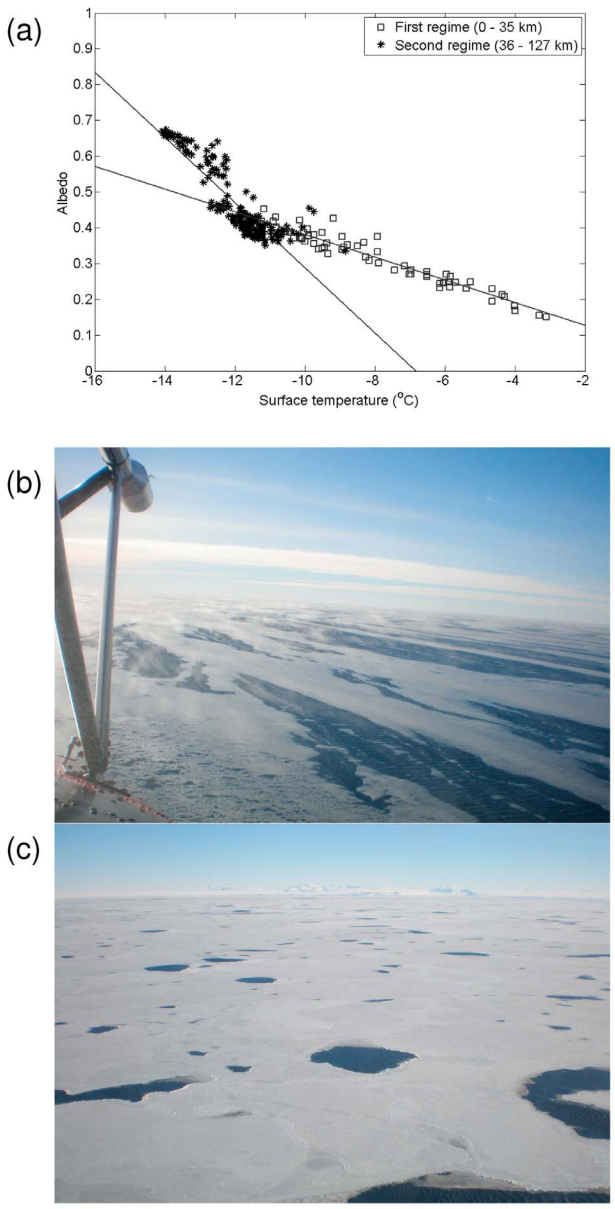

Figure 3. (a) 1 km averaged shortwave albedo and surface temperature for F54L1 and F54L2, split into regimes where first regime is the first 35 km. Photographs of ice conditions observed within (b) first regime and (c) second regime during F54.

evident in the similarity of the gradient of the best fit line between the flight legs at −0.03 for F54L1 and F54L2 and −0.04 for F57L1. This similarity is not seen for the second regime.

[36] Figure 3 also shows photographs of the surface conditions observed within each regime for F54 as an example. The first regime (Figure 3b), i.e., the active polynya, is composed of open water and frazil ice. Langmuir circulations can be observed in the surface distribution pattern of the frazil ice and ice fog can also be seen. New ice, which appeared to be thicker and contained open water patches or "holes," was also observed within this regime. The second regime (Figure 3c), the young ice region, is composed of more consolidated ice, also perforated with "holes." Leads and ridging of the ice floes were also observed within this region. The two regimes can be clearly seen on Figure 4, an image of sea ice concentration derived from AMSR-E (Advance Microwave Scanning Radiometer for EOS) data for the day of F54.

[37] The perforated appearance of the ice is due to cold air temperatures and rapid advection of the newly formed frazil ice, which consolidates into floes before it can be piled up against the receding edge of the polynya [*Smith et al.*, 1990]. Owing to reduced turbulence, the ice production rate within these holes is lower than in the more open areas in the sea ice cover, where Langmuir circulations were observed. Consolidation of the frazil into floes is therefore less efficient, and thus, the holes remain open [*Smith et al.*, 1990].

3.3. Vertical Profiles

[38] Figure 5 shows cross sections of potential temperature, specific humidity, wind speed, and wind direction over the Ronne Polynya, using the sawtooth profile data collected during F57. The profile data were averaged over 10 s intervals before interpolation between points and contouring. The interpolation was achieved using the Matlab "griddata" function, whereby a surface is fitted to the non-uniformly spaced fetch, height, and variable data. Using a triangle-based linear interpolation method, values of the variable are then interpolated at the points specified by a uniform two-dimensional grid of fetch and height.

[39] The growth of a well-mixed CIBL resulting from the surface temperature discontinuity at the ice shelf edge is evident in the cross sections of potential temperature, specific humidity, and wind speed (Figure 5). The top of the CIBL, z_i, is marked in Figure 5. Following *Melfi et al.* [1985], *Chou and Zimmerman* [1989], and *Grossman and Betts* [1990], z_i has been defined as the height of the base of the capping inversion layer (the entrainment zone) above the mixed layer, i.e., the vertical limit of the mixed layer. z_i has been determined subjectively from vertical profiles of

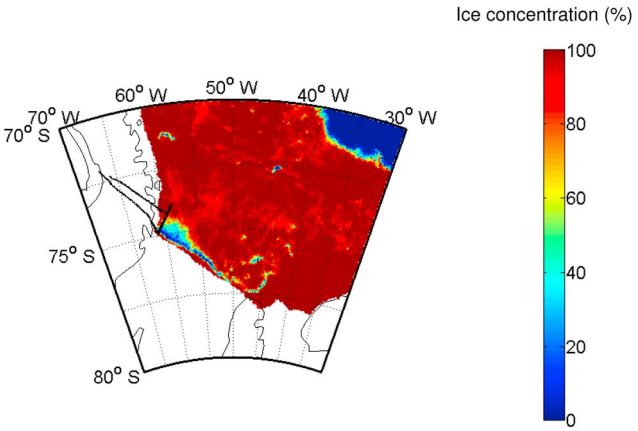

Figure 4. AMSR-E sea ice concentration in the Weddell Sea, 27 February 2007 (day of F54). Data are from http://iup.physik.uni-bremen.de:8084/amsr/amsre.html [*Spreen et al.*, 2008]. Low ice concentrations can be seen at the Ronne Polynya (around 75°S, 60°W), where the two ice regimes can be observed. Entire flight track for F54 shown in black on image.

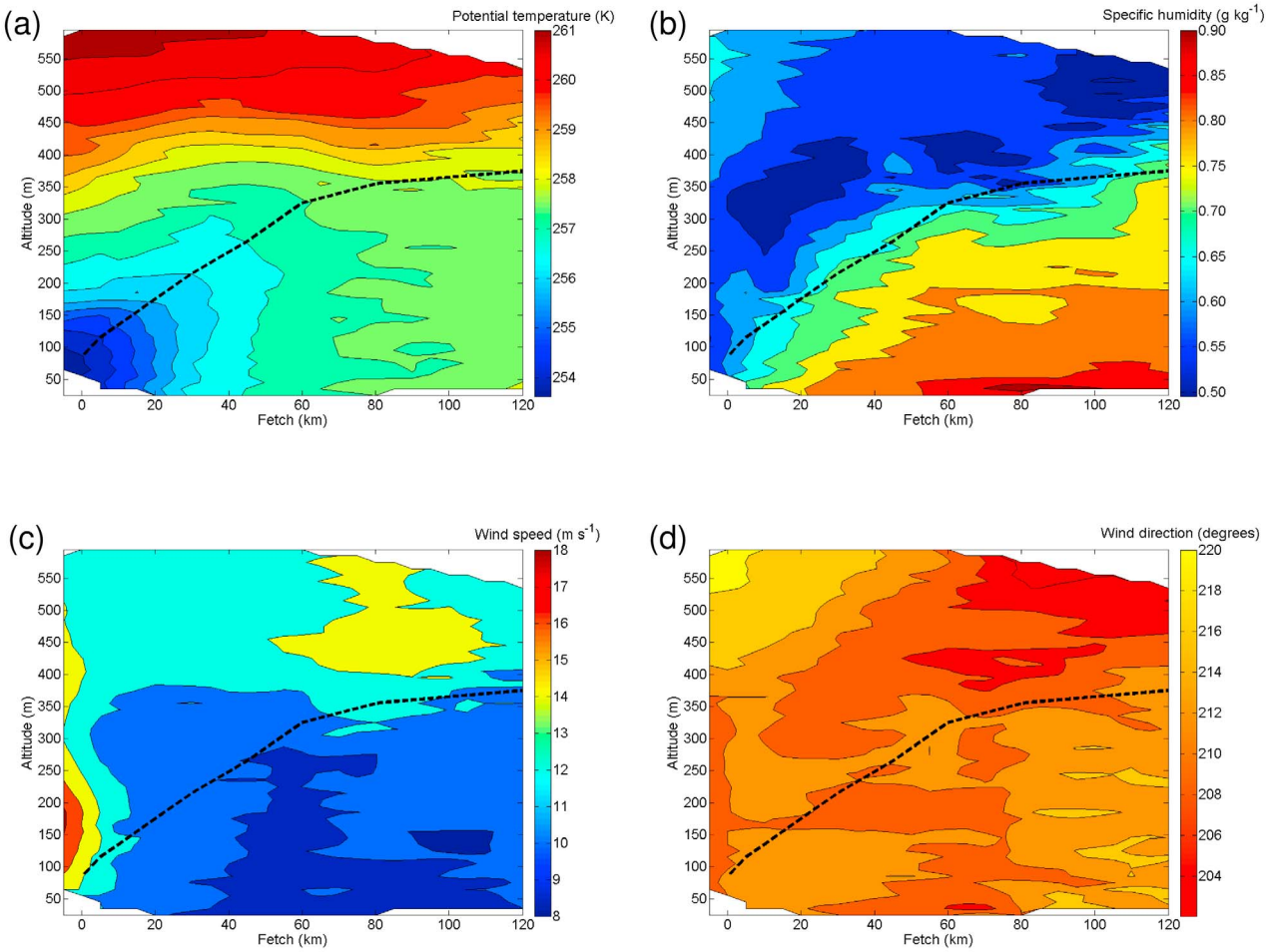

Figure 5. Contoured cross-sections above Ronne Polynya, during F57 (28 February 2007). x = 0 km is edge of Ronne Ice Shelf, and z = 0 m is polynya surface. z_i (convective internal boundary layer top) estimated from potential temperature contour plot (see text) and shown on all plots as dashed black line: (a) potential temperature, (b) specific humidity, (c) wind speed, and (d) wind direction.

potential temperature and corresponds to the abrupt change in stability from neutral within the CIBL to stable within the entrainment zone. The CIBL depth increases with fetch from the ice shelf edge (Figure 5), due mostly to warming as a result of sensible heat flux convergence from the polynya surface but also partially to the entrainment of warm air from above the CIBL [*Garratt*, 1990].

[40] A strong gradient of potential temperature and specific humidity with fetch can be seen as the CIBL warms and moistens, particularly over the initial 30 km or so (Figure 5). Moisture also decreases with height within the CIBL as a result of the addition of moisture from the surface and the entrainment of dry air from above [*Stull*, 1988] and remains approximately constant above the level of z_i. The measured wind speed is almost constant within the CIBL, increasing above it, which indicates the CIBL is very well mixed. The higher wind speed feature positioned over the ice shelf is unexpected. This is perhaps a temporal rather than spatial feature (i.e., the wind speed was increasing overall during this final profile) but could warrant further investigation. The wind direction is fairly constant, not just within the CIBL but for the entire cross section. The internal boundary layer can be seen on the potential temperature cross section (Figure 5a) to merge into the planetary boundary layer after about 80 km fetch.

[41] Similar sawtooth profile-derived cross sections have been examined for F54 (not shown). The results are qualitatively similar to those illustrated in Figure 5. Further details are provided in *Fiedler* [2009].

3.4. Sensible Heat Flux

[42] It is assumed that fluxes measured during the low-level flight legs (between 14 and 33 m) are representative of surface values. That is, the aircraft was flying within the surface layer and thus extrapolation of the flux values to the surface was not necessary. An unstable surface layer can be observed in the vertical potential temperature profiles (Figure 5a), the depth of which is greater than the data collection altitude for these flight legs, supporting this assumption.

[43] Figure 6 shows the eddy covariance sensible heat flux over the Ronne Polynya with fetch from the ice shelf edge at 0 km for the four level flight legs. Also shown are the flight level potential temperature, surface temperature, and surface

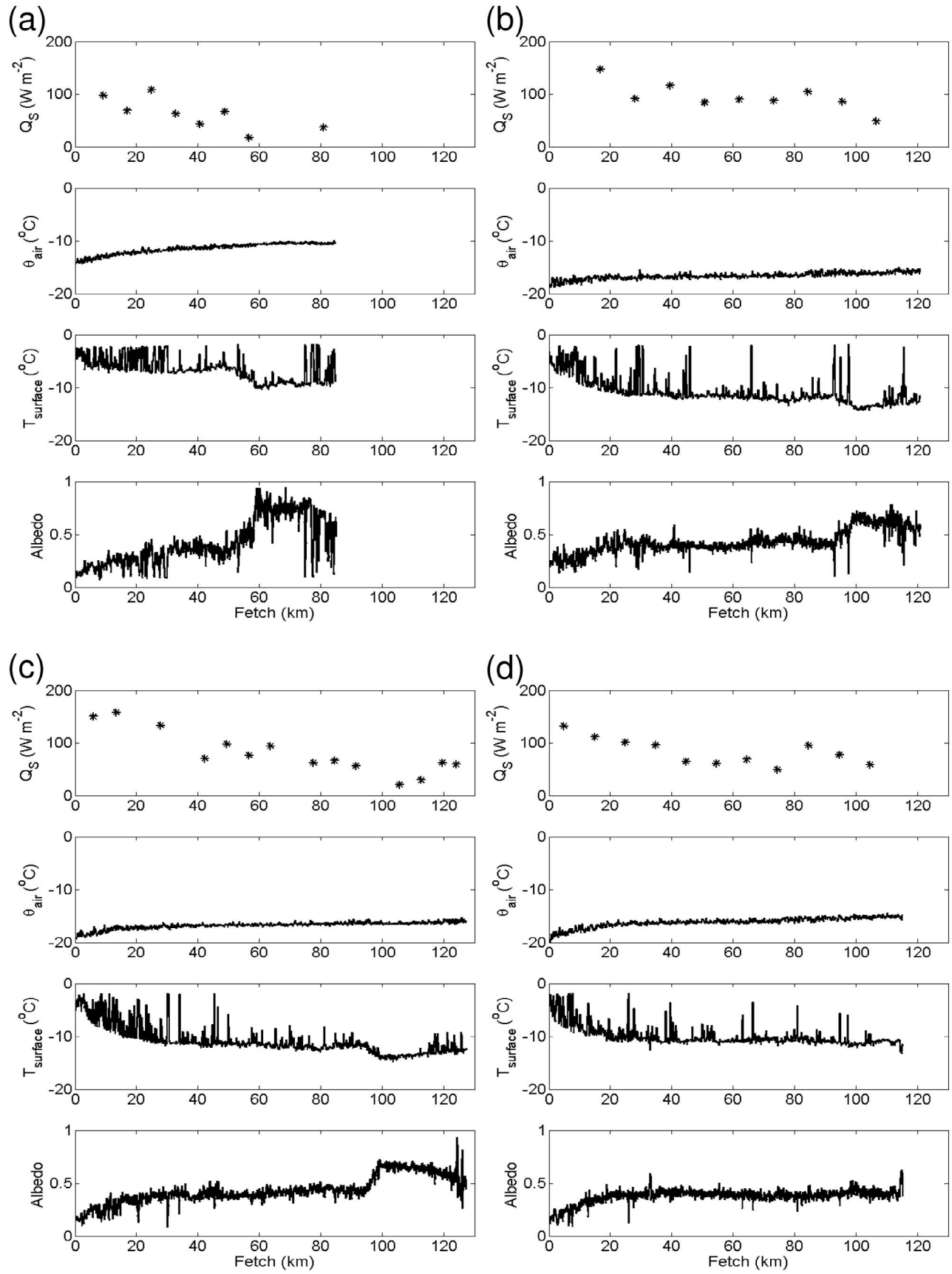

Figure 6

Table 3. Measured Sampling Error in $\overline{w'T'}$ and Measured Values of the Empirical Constant α_F, for Calculation of the Predicted Sampling Error, All Obtained Using Equation (9)

Flight	Measured Sampling Error (%)	α_F	Measurement Altitude (m)
F49L2	32	5.3	32
F54L1	20	5.0	14
F54L2	27	4.4	33
F57L1	22	5.3	15

shortwave albedo for each leg. For all legs, the surface temperature decreases with increasing fetch, while albedo increases, suggesting that ice thickness increased with fetch. Patches of thin ice and open water within the generally thicker ice are also apparent from these plots.

[44] A decrease in the observed surface sensible heat flux with fetch is seen for all legs on Figure 6, resulting from a reduction in the air-surface temperature difference. This is due in part to warming of the CIBL (of around 4 K over the polynya fetch) by sensible heat flux convergence. However, the reduction in surface temperature with fetch of typically 9 K, as a result of the thickening ice cover, was greater than the air temperature increase (Figure 6). Therefore, for this case, variation in the temperature of the heterogeneous surface has the greatest effect on the spatial variability of the sensible heat flux.

[45] The magnitude of the sensible heat flux over the second regime (section 3.2) is on the order of 100 W m^{-2}, which is larger than would be expected over consolidated sea ice. Therefore, the definition of the polynya area used in this study includes this second "young ice" regime. The outer edge of the polynya is indicated by a sharp increase in the surface albedo, at 60 km for F49 and 100 km for F54. The edge of the polynya was not reached for F57.

3.4.1. Flux Sampling Error

[46] Under stationary conditions, the sampling error of a turbulent flux (e.g., $F = \overline{w'T'}$) can be expressed as [*Donelan*, 1990; *Drennan et al.*, 2007],

$$\frac{\sigma_F}{\overline{F}} = \alpha_F z^{1/2} U^{-1/2} \gamma^{-1/2}. \quad (9)$$

Applying this to the Ronne Polynya data, for each low-level flight leg σ_F is the standard deviation of flux estimates for all runs of that leg (after quality control) and $\overline{F}$ is the mean of these flux estimates. α_F is an empirically derived constant, the value of which is dependent on the type of flux being measured and on the stability conditions. z is the measurement altitude in m, U is the speed of advection of turbulence past the probe in m s^{-1} (equivalent in this case to the level flight true air speed of the plane, 63 m s^{-1}), and γ is the sampling interval in seconds (which is the averaging interval of the data, 140 s). The left-hand side of equation (9) represents the measured sampling error, and the right-hand side represents the predicted sampling error. The equation demonstrates that lower measurement heights, faster fluid speeds relative to the measuring apparatus, and longer averaging periods will yield less scattered results, i.e., a reduction in the variability of the results.

[47] Equation (9) was used to calculate the measured sampling error for the kinematic sensible heat flux for each of the four low-level flight legs. Results are given in Table 3. A linear fit of the flux was removed before calculation of the standard deviation as an approximation of the expected reduction in the flux with fetch not due to error in the data. The data were also used to calculate values for the empirical constant α_F (also given in Table 3) for these unstable convective conditions, which could be used in future investigations to predict the sampling error. This is a useful calculation as a measured sampling error which is considerably larger than that predicted is a likely indication of nonstationary conditions [*Drennan et al.*, 2007]. Using data from all four flux legs gives a mean value for this constant of 5.0. As would be expected, this is lower than the value given by *Donelan* [1990] of 8.0, which was appropriate for near-neutral stratification.

[48] As the L2s were conducted at a higher altitude, a larger scatter in the data is both expected and found in comparison with the L1s. This sampling error could be reduced by, for example, increasing the length of the averaging period, which would also improve the spectra of the data. The number of runs which are rejected would then be reduced (section 2.3), but at the expense of capturing the spatial variation in the surface fluxes. However, these sampling errors are of a similar magnitude to those found in other studies [*Drennan et al.*, 2007; *Petersen and Renfrew*, 2009] and additionally some scatter in data from measurement of turbulent quantities is expected. Nevertheless, in order to produce results that are as accurate as possible, data from the L1s only were used in the following section for the calculation of surface transfer coefficients.

3.5. Surface Transfer Coefficients

[49] The 10 m neutral stability heat transfer (C_{HN10}) and drag (C_{DN10}) coefficients were calculated using the method detailed in section 2.2.2 for each 8.8 km run for both F54L1 and F57L1. They are shown on Figure 7 with fetch from the ice shelf edge at 0 km. Despite the data being collected more than 24 h apart, for both legs the mean values and standard deviations of these coefficients are the same, at $C_{DN10} = (1.1 \pm 0.2) \times 10^{-3}$ and $C_{HN10} = (0.7 \pm 0.1) \times 10^{-3}$. This indicates that even for the dynamic system of a coastal polynya, where the surface varies between open water, new ice, and more consolidated ice, the surface roughness length across the polynya remains effectively constant.

[50] The magnitudes of these coefficients compare very well to similar aircraft-based observations made by *Schröder et al.* [2003] over heterogeneous sea ice in the Arctic marginal ice zone (MIZ). For the ice class they defined as a mixture of gray and white ice and leads, which is comparable to the surface of the Ronne Polynya, they obtained mean values of $C_{DN10} = (1.5 \pm 0.5) \times 10^{-3}$ and $C_{HN10} = (0.8 \pm 0.2) \times 10^{-3}$. The observed C_{HN10} values at

Figure 6. For flight legs (a) F49L2, (b) F54L1, (c) F54L2, and (d) F57L1, top to bottom: eddy covariance sensible heat flux, potential temperature, surface temperature, and surface shortwave albedo, all with fetch from ice shelf edge at 0 km. The mean altitudes of flight legs are F49L2 (32 m), F54L1 (14 m), F54L2 (33 m), and F57L1 (15 m).

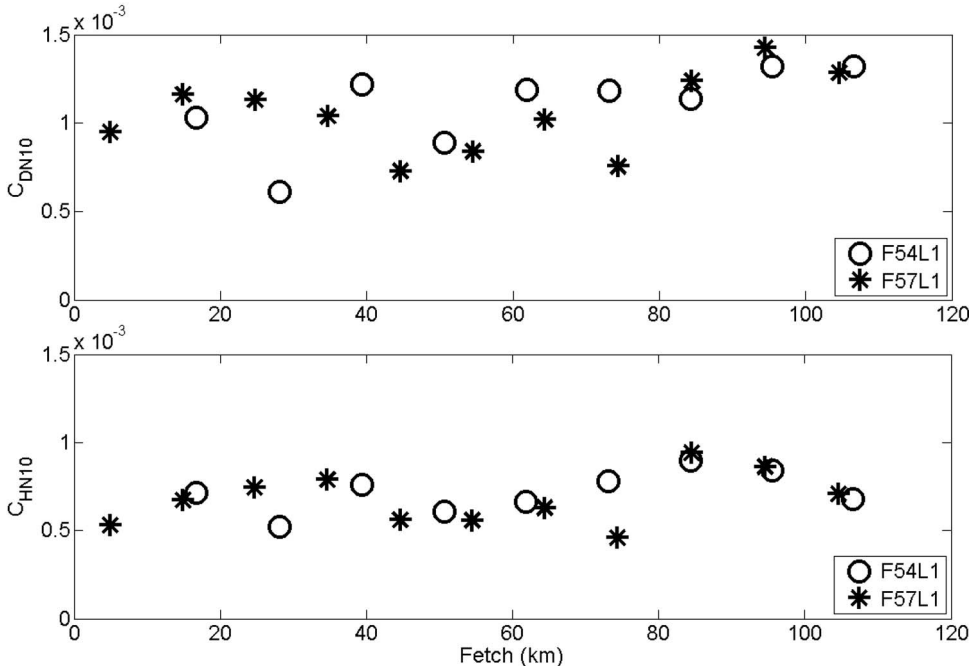

Figure 7. (top) 10 m neutral stability drag and (bottom) heat transfer coefficients for F54L1 and F57L1.

the Ronne Polynya are significantly lower than those normally used in studies of turbulent heat transfer over polynyas, e.g., *Chapman* [1999] and *Walkington and Willmott* [2006] at 2.0×10^{-3} or *Renfrew et al.* [2002] at 1.14×10^{-3}. However, the coefficients obtained in this study of the Ronne Polynya are relevant to conditions of thin ice cover rather than open water which is often assumed to be the case when modeling polynyas. The magnitude of the drag coefficient obtained in this study is similar to that used in previous studies, e.g., 1.0×10^{-3} [*Renfrew et al.*, 2002].

3.6. Relationships Between Surface Transfer Coefficients and Ice Conditions

[51] Despite the steadily increasing thickness of the ice cover with fetch, as implied by the surface temperature and albedo plots (Figure 6), there is no corresponding change in C_{DN10} and C_{HN10} (Figure 7), i.e., using data from F54L1 and F57L1 together, the regression of C_{DN10} and C_{HN10} with fetch does not have a slope significantly different from zero. Note that, if C_{DN10} for F54L1 is examined alone, the slope is found to be significantly different from zero, at the 0.05 significance level. This is not the case for F57L1 or for C_{HN10} for either leg. However, F54L1 comprises only 9 data points and therefore examination of the two legs together is likely to produce a more statistically robust result. Therefore, it can be concluded that there is no variation with fetch in either C_{DN10} or C_{HN10}. This at first appears to be a surprising result, given the presumed thickening of the ice cover with fetch. However, the sea ice roughness (and hence C_{DN10}) cannot be characterized by a single parameter such as ice thickness alone but includes other factors such as floe size, freeboard and concentration, and small variations in these do not necessarily alter momentum exchange [*Schröder et al.*, 2003]. In addition, form drag does not affect heat exchange directly [*Schröder et al.*, 2003], so even with a large variation in surface roughness a relationship with C_{HN10} would not necessarily be seen.

[52] Removal of the single point of the transfer coefficients for F54L1 that lies outside the outer edge of the polynya (section 3.4) does not alter the mean, standard deviation, or fetch correlations for C_{DN10} or C_{HN10}.

[53] A *t* test shows there is no significant difference between the means of C_{HN10} for the two regimes, established by the surface temperature and albedo conditions (Figure 3). For F54L1, there appears to be a significant difference at the 0.05 significance level between the means for C_{DN10}. However, for this leg, the first regime comprises of only two points and therefore this result should be treated with caution, especially as the same result is not found for F57L1. When the data from both legs are considered together, thus forming a larger data set, there is no significant difference in either C_{HN10} or C_{DN10} between the regimes.

[54] Using the surface temperature and surface shortwave albedo as indicators of the surface ice conditions, the relationships between these factors and the calculated transfer coefficients were also investigated (Figure 8). No significant correlations were found between the transfer coefficients and either the albedo or the surface temperature, both when considering all the data together, and under separate analysis of the two regimes.

[55] It can thus be concluded that, for this case study, the heat transfer coefficients for the two regimes are the same. This suggests that under similar polynya conditions to those observed, the two ice regimes can be treated in the same way when modeling the surface heat fluxes.

4. Investigations Using a Simple CIBL Model

4.1. The Model

[56] The convective internal boundary layer (CIBL) model of *Renfrew and King* [2000] was used to investigate

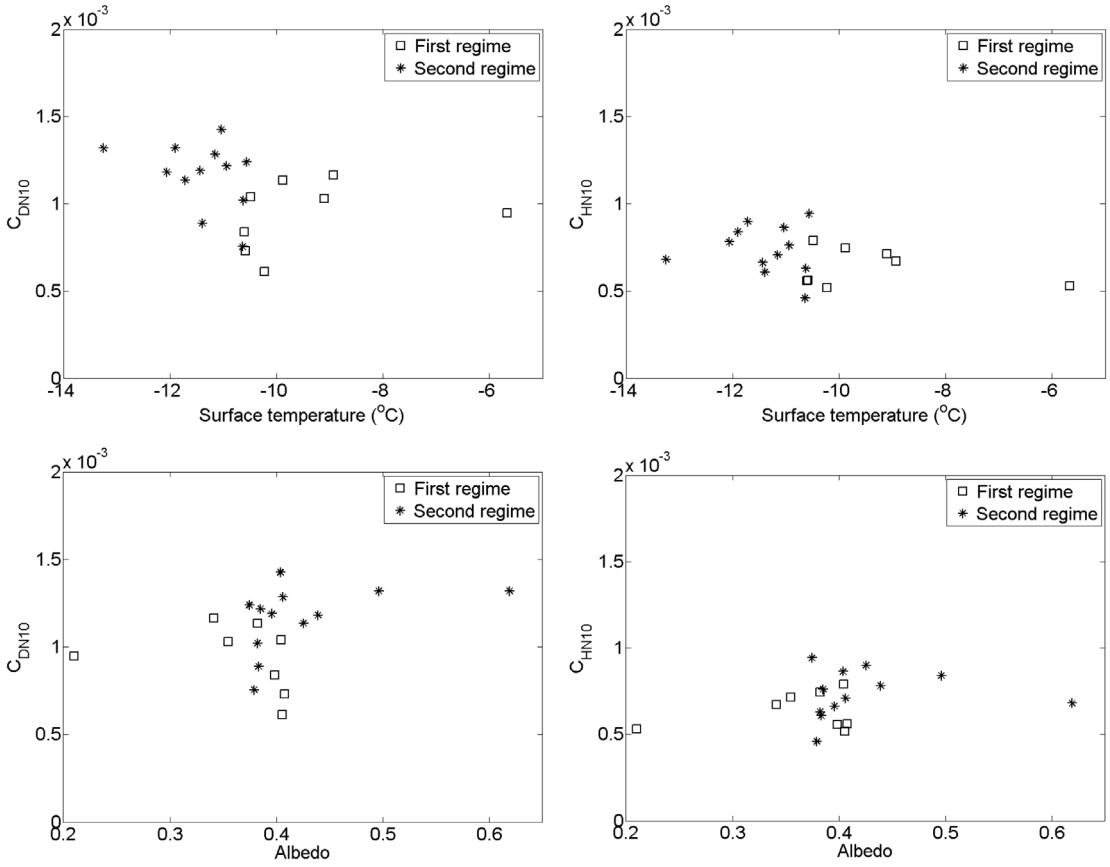

Figure 8. F54L1 and F57L1 (left) 10 m neutral stability drag coefficients and (right) sensible heat transfer coefficients with (top) surface temperature and (bottom) surface shortwave albedo. Data split into two ice regimes, as in Figure 3.

the evolution with fetch of the surface sensible heat flux, mixed layer potential temperature, and CIBL depth over the Ronne Polynya. This one-dimensional, zero-order jump model was designed to investigate the systematic and nonuniform modification of surface turbulent heat fluxes with fetch over polynyas.

[57] The model equations dictate that sensible heat flux convergence is responsible for warming of the boundary layer over the polynya. The variation in the surface flux therefore controls downwind changes in boundary layer depth and potential temperature, under steady state conditions. Given inputs of wind speed, surface and mixed layer temperatures, plus estimates of the initial boundary layer depth, ambient atmospheric stability and the entrainment parameter (ratio of the entrainment heat flux at the top of the boundary layer to that at the surface), which have previously been assigned climatologically, the model is then able to estimate the surface sensible heat flux, potential temperature, and development of the CIBL depth with polynya fetch. Full model details are given in the work of *Renfrew and King* [2000].

[58] It is inaccurate to assume heat fluxes over polynyas are constant over mesoscale fetches [*Smith et al.*, 1990; *Pinto et al.*, 1995] and it is therefore important to include a developing boundary layer when modeling the turbulent heat fluxes with fetch. This model, which is appropriate for the investigation of cloud-free CIBLs and allows the surface sensible heat flux, mixed layer potential temperature, and boundary layer depth to vary nonlinearly with fetch, is therefore suitable for use in this study of the ocean-atmosphere sensible heat flux over the Ronne Polynya.

4.2. Modeling of Ronne Polynya Case Studies

[59] The observational data collected over the Ronne Polynya during F54 were used to provide the initial model conditions at a fetch of 0 km (the ice shelf edge). The parameters used for the model runs are given in Table 4. These values include atmospheric stability above the CIBL (γ_θ), which was estimated from the contour plot of potential temperature with height for this flight (not shown, see *Fiedler* [2009] for details) and the entrainment parameter (β), which was calculated using observations of the jumps in potential temperature and wind speed across the top of the CIBL, following *Stull* [1988]. Details of this calculation are also given in the work of *Fiedler* [2009].

[60] The model was designed for the simple case of an open water polynya with a constant surface temperature, at the freezing point, where variation in the air temperature leads to variation in the surface sensible heat flux with fetch. However, as discussed above, at the time of the observations the Ronne Polynya was mostly covered with thin ice, which increased in thickness with fetch causing a reduction in the measured surface temperature. As demonstrated, this had a greater effect on the spatial variation of the sensible heat

Table 4. Model Input Data From Aircraft Observations for Flight F54 Simulation

Wind Speed	θ_{air}	T_{sfc} Regime 1	T_{sfc} Regime 2	Pressure	Ambient Stability	Entrainment Parameter
17 m s^{-1}	−18.8°C	−7.8°C	−11.7°C	994 mb	6 K m^{-1}	0.5

flux than did variations in the air temperature (section 3.4). A two-regime surface temperature was therefore introduced to the model, using the observed mean value for each regime to take some account of the variation in surface temperature with fetch.

[61] In addition, the mean values of the transfer coefficients obtained for the Ronne Polynya of $C_{HN10} = 0.7 \times 10^{-3}$ and $C_{DN10} = 1.1 \times 10^{-3}$, which were found to be valid for both regimes, were introduced to the model. These replaced the model default values appropriate for open water [*Renfrew and King*, 2000] of $C_{HN10} = 1.14 \times 10^{-3}$ [*DeCosmo et al.*, 1996] and $C_{DN10} = 1.0 \times 10^{-3}$ [*Smith*, 1988].

[62] The modeled surface sensible heat flux, mixed layer potential temperature, and CIBL depth were then compared with the Ronne Polynya observations.

4.2.1. Surface Sensible Heat Flux

[63] The model was run using a two-regime surface temperature as well as a one-regime surface temperature for comparison. In addition, the model was also run assuming the polynya consisted of open water at the freezing point (as was done by *Renfrew et al.* [2002]) at an appropriate constant surface temperature of −1.9°C [*Nicholls et al.*, 2004]. First, the original model transfer coefficients for open water were used, followed by the Ronne Polynya transfer coefficients for comparison. Results are all shown on Figure 9, along with the observed eddy covariance sensible heat flux for F54L1 and F54L2. The magnitude of the error bars given for the observations are obtained from the measured sampling error (Table 3). A measured sampling error of e.g., 20% (F54L1) corresponds to an error in the data of potentially ±10%.

[64] It can be seen on Figure 9 that the modeled sensible heat flux is not only very sensitive to the prescribed surface temperature but also to the value of the transfer coefficients (primarily C_{HN10} owing to the large difference between the DeCosmo C_{HN10} and that observed). Therefore, errors in either the surface temperature or the heat transfer coefficient could result in a large overestimate or underestimate of the magnitude of the modeled surface sensible heat flux at the Ronne Polynya.

[65] Table 5 shows the root mean square (RMS) errors for each of these modeled sensible heat fluxes compared to the observed eddy covariance sensible heat flux. Also included in Table 5 are the RMS errors for model runs using the observed mean surface temperature for each 1 km point, for both F54L1 and F54L2.

[66] The model runs using the observed surface temperature together with the observed transfer coefficients give, as would be expected, the best result when compared with the observed eddy covariance heat flux. However, the two-regime surface temperature produces a result of only slightly reduced accuracy in comparison (Table 5 and solid line, Figure 9). In contrast, a single regime, i.e., a constant surface

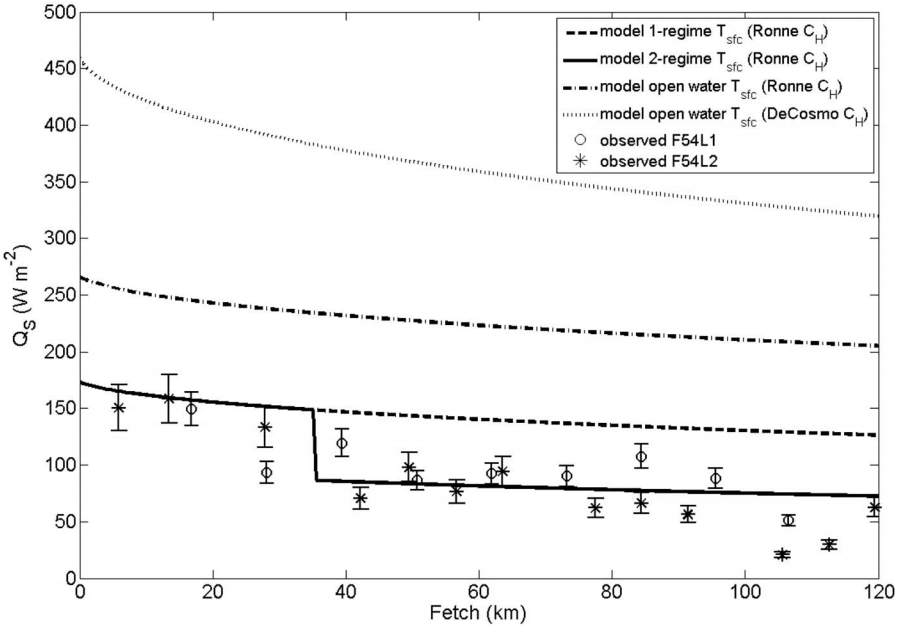

Figure 9. Model runs of sensible heat flux over the Ronne Polynya, showing the effect of variations in both surface temperature (T_{sfc}) and heat transfer coefficient (C_H). Values used are given in Table 5. Observed eddy covariance sensible heat flux for flight legs F54L1 and F54L2 (error bars from sampling error, Table 3) shown for comparison.

Table 5. Flight F54 RMS Errors for Model Runs of Sensible Heat Flux[a]

T_{sfc}	C_{HN10}	RMS error (W m^{-2})
1 regime (−18.8°C)	Ronne (0.7×10^{-3})	59.6
2 regime (−7.8°C, −18.8°C)	Ronne (0.7×10^{-3})	24.5
Open water (−1.9°C)	DeCosmo (1.14×10^{-3})	273.5
Open water (−1.9°C)	Ronne (0.7×10^{-3})	138.4
F54L1 observed (1 km means)	Ronne (0.7×10^{-3})	22.1
F54L2 observed (1 km means)	Ronne (0.7×10^{-3})	21.3

[a]Using different surface temperatures (T_{sfc}) and sensible heat transfer coefficients (C_{HN10}). Observations used for comparison are the eddy covariance sensible heat flux for low-level legs of F54 (F54L1 and F54L2) together.

temperature based on the temperature over the first 35 km only, significantly increases the RMS error (Table 5 and dashed line, Figure 9). Therefore, the two-regime method preserves the simplicity of the model, while giving comparable results to inputting the surface temperature at each point. This is useful for modeling applications where high-resolution surface data may not be available. Furthermore, it is possible the surface temperature could be determined from satellite measurements on these spatial scales. For a two-regime polynya, a mean surface temperature over the whole polynya is close to the temperature over the longer second regime and so does not capture the magnitude of the heat flux over the first regime if used in the model.

[67] The use of a two-regime surface temperature has a less important effect on the modeled heat fluxes for F57, reducing the RMS error by only 2 W m^{-2} compared to the single regime (not shown here, see *Fiedler* [2009]). This is because there is a smaller surface temperature difference between the two regimes for F57 (1.4°C compared to 3.9°C for F54). Therefore, the importance of a two-regime temperature input is dependent upon the magnitude of the difference between the mean surface temperatures of the two regimes.

[68] Figure 9 illustrates that the difference in the modeled sensible heat flux between using an open water surface temperature and an ice surface temperature is significant. It also indicates the importance of using the correct magnitude of the heat transfer coefficient. This is the case for both F54 and F57. However, for F49, using an open water surface temperature does not produce results as inaccurate as for the other two flights. The RMS error for the modeled sensible heat flux, using the observed transfer coefficients, is 26.3 W m^{-2} for the observed mean surface temperature of −6.9°C (two separate regimes were not found for F49, see section 3.2) and for open water at −1.9°C is 29.9 W m^{-2}. The open water surface temperature is closer to that observed than for the other flights. Additionally, the reduced magnitude of the heat flux for this flight means the error is proportionally smaller. However, the sensible heat flux is greatly overestimated when using a heat transfer coefficient appropriate for open water, along with the open water surface temperature, where the RMS error amounts to 72.7 W m^{-2}.

4.2.2. Potential Temperature

[69] Figure 10a shows the modeled potential temperature (θ) with polynya fetch along with the mean observed for the two low-level legs of F54. Using an ice surface temperature and the Ronne Polynya heat transfer and drag coefficients, the model captures the change in θ with fetch very well. For the two-regime surface temperature the RMS error between the modeled and observed θ (the mean of the θ observations for F54L1 and F54L2) amounts to 0.17 K; slightly lower than the 0.34 K found for the one-regime. Results were similar for F57, where a two-regime surface temperature resulted in a slight improvement in the modeled variation in θ compared with that observed. However, this improvement was smaller than that found for F54, with an RMS error of 0.34 K for the one-regime surface temperature compared with 0.31 K for the two-regime surface temperature.

[70] The greatest increase in the magnitude of the RMS error was found for both cases when a surface temperature (−1.9°C) and heat transfer coefficient (1.14×10^{-3}) [*DeCosmo et al.*, 1996] appropriate for open water were used for the model runs. This produced an RMS error of 1.69 K for F54 and 2.11 K for F57. Again, this illustrates the importance of using a surface temperature and transfer coefficients appropriate for a surface covered with thin ice for accurate modeling.

4.2.3. CIBL Depth

[71] Figure 10b shows the modeled CIBL depth (z_i) with fetch over the Ronne Polynya for F54 compared to the observed z_i, derived from potential temperature profiles as discussed in section 3.3. Using the two-regime surface temperature, the model captures the observed CIBL development well, with an RMS error of 10.3 m. The one-regime surface temperature parameterization led to an RMS error of 33.2 m.

[72] For F57, the RMS error of the modeled z_i is 14.9 m using a one-regime surface temperature and, marginally worse, at 16.2 m for a two-regime surface temperature. This demonstrates that, as above for the surface sensible heat flux and potential temperature, the use of a one-regime or two-regime temperature parameterization does not greatly affect the accuracy of the model results for the F57 case owing to the small temperature difference between regimes.

[73] Again, for both flights, the RMS error is increased for the model runs using an open-water surface temperature and transfer coefficients. This RMS error amounts to 280.7 m for F54 and 174.6 m for F57.

[74] The modeled boundary layer depth is very sensitive to the input value of the ambient stability, i.e., the stability above the growing CIBL, and to a lesser degree the entrainment parameter [*Renfrew and King*, 2000]. The methods described previously by which the values used in this study (Table 4) were obtained appear to have been appropriate, however, given the excellent fit of the modeled z_i to the observations.

[75] The initial value of the modeled boundary layer depth at 0 km, which takes into account the depth of the mechanically driven boundary layer above the ice shelf, was set to 85 m above the polynya surface. This was the value

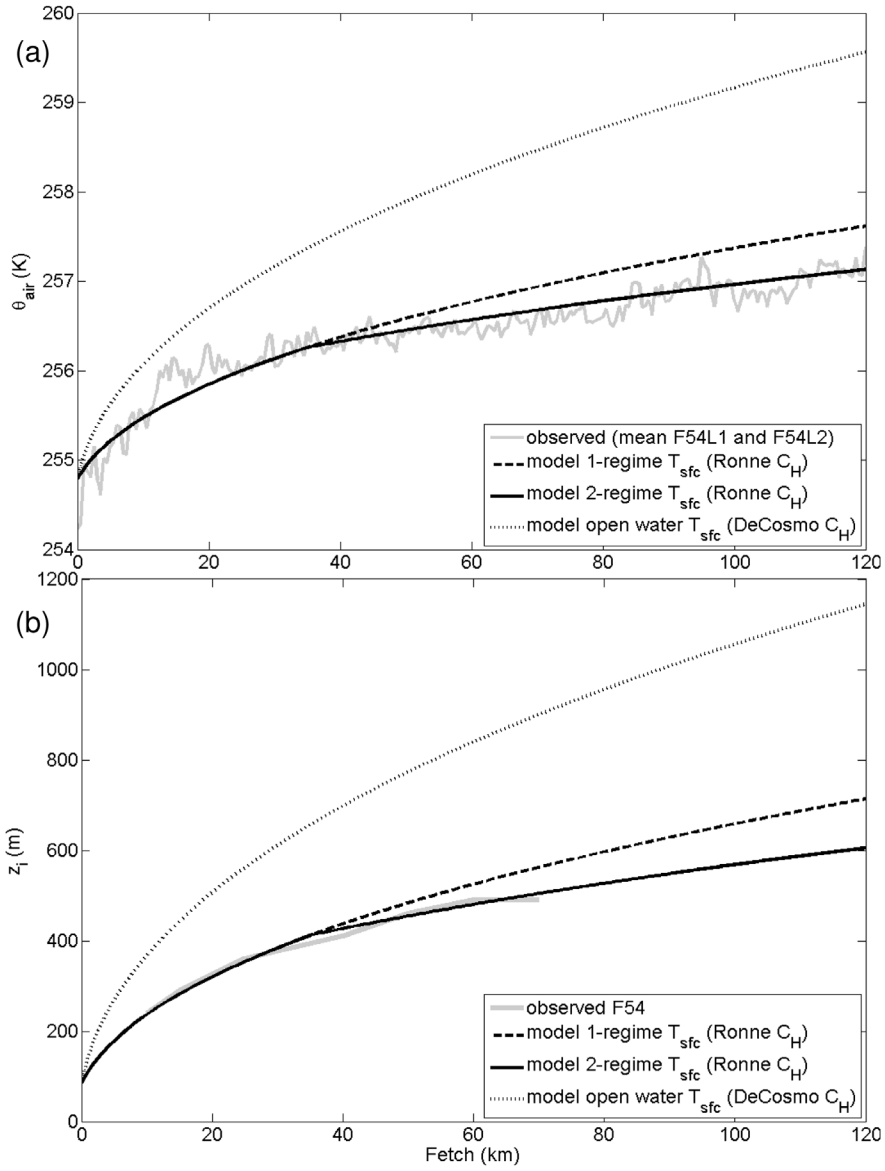

Figure 10. (a) Modeled and observed potential temperature (θ) and (b) convective internal boundary layer depth (z_i) for flight F54 shown with fetch over the Ronne Polynya. Observed θ is mean of low-level legs F54L1 and F54L2, averaged over 0.5 km sections.

observed for F57 as no measurements of this parameter were obtained for F54. This could be a source of error, given that the wind speeds during F54 were stronger than for F57, which would suggest a deeper boundary layer. However, the modeled evolution of z_i, as well as θ, and the sensible heat flux are not particularly sensitive to this parameter [*Renfrew and King*, 2000], and Figure 10b suggests the chosen value was appropriate.

5. Discussion and Conclusions

[76] Convective heat transfer at an Antarctic coastal polynya, the Ronne Polynya, has been investigated through field observations and modeling. Three flights, comprising four low-altitude, straight and level legs and two sawtooth pattern profiling legs, were conducted over the polynya using an instrumented aircraft. At the time of the observations the polynya was mostly covered with thin ice. Using the surface temperature and albedo measurements, the area can be split into the two distinct regimes referred to by *Liu et al.* [1997] as the "active polynya" and "young ice" regions. On the basis of visual observations from the aircraft, the first regime was found to be composed of open water, frazil ice, and some thicker new ice, perforated with open water patches or "holes." The second regime was composed of more consolidated ice, also perforated with "holes." Leads and ridging of the ice floes were observed within this region.

[77] The eddy covariance sensible heat flux over the polynya was found to decrease with fetch from the edge of the ice shelf, owing to a reduction in the surface-air temperature difference. This was primarily a result of variation in the surface ice cover which, as indicated by a decrease in surface temperature and an increase in the shortwave albedo,

increased in thickness with fetch. There was also some contribution from warming of the air due to sensible heat flux convergence.

[78] The mean 10 m neutral stability sensible heat transfer and drag coefficients at this time were $C_{HN10} = (0.7 \pm 0.1) \times 10^{-3}$ and $C_{DN10} = (1.1 \pm 0.2) \times 10^{-3}$, where the errors given are the standard deviations. The magnitude of this heat transfer coefficient is significantly lower than has been previously used in studies of heat fluxes over polynyas, which are often assumed to be open water, e.g., 1.14×10^{-3} [*Renfrew et al.*, 2002] or 2×10^{-3} [*Chapman*, 1999; *Walkington and Willmott*, 2006]. It is instead similar to that found over a heterogeneous ice surface in the Arctic MIZ by *Schröder et al.* [2003] of $(0.8 \pm 0.2) \times 10^{-3}$. This similarity also indicates these data are not applicable solely to the investigation of heat transfer at polynyas but to other regions of heterogeneous ice cover. The surface transfer coefficients were found not to be a function of polynya fetch, despite the increasing thickness of the ice cover. Furthermore, no significant difference between the values of the coefficients for the two ice regimes was found, which suggests the process of heat transfer is similar for the two regimes. This implies that, under similar conditions to those observed, the two ice regimes can be treated in the same way when modeling the surface sensible heat flux.

[79] The sensible heat flux observed over the second regime was larger than would be expected over consolidated pack ice, as a result of perforations within the ice. This finding, coupled with the similarity between the two regimes of both the heat transfer and drag coefficients, means the second regime was also considered to be part of the polynya. Frazil ice formation rates are predicted to be lower within these perforations than in more extensive areas of open water as a consequence of the reduction in wind-generated turbulence [*Smith et al.*, 1990]. Nevertheless, the magnitude of the sensible heat flux means the investigation of wintertime ice production and dense water formation within this regime will be of importance. This, along with the growth of congelation ice on the underside of the consolidated ice should therefore be considered in addition to the ice production rate of the more widely recognized first regime. The Ronne Polynya is a typical coastal polynya, and hence, the conclusions drawn from this study are applicable to other coastal polynyas in both the Arctic and Antarctic, under conditions where they are covered with thin ice.

[80] The observations obtained at the Ronne Polynya were used as input parameters for a simple model of the CIBL over a wind-driven polynya during a cold air outbreak, devised by *Renfrew and King* [2000]. It was shown that, given appropriate input parameters including representation of the surface temperature difference between the two ice regimes where necessary, the model was able to accurately capture variations with fetch in the surface sensible heat flux, potential temperature, and CIBL depth with RMS errors as low as 24.5 W m^{-2}, 0.17 K, and 10.3 m, respectively. The model would not be expected to capture the variability inherent in the data exactly, and this is therefore an excellent result.

[81] The use of a surface temperature and heat transfer coefficient appropriate to an ice-covered surface was found to be necessary for accurate modeling of the sensible heat flux, potential temperature, and CIBL depth for the Ronne Polynya case study, particularly when the surface-air temperature difference was large. This suggests that under conditions where significant ice cover is expected, for example, under similar conditions to those observed, the heat flux over any coastal polynya should be modeled in this way.

[82] Numerous modeling studies of coastal polynyas have been based on the assumption that newly formed frazil ice within the polynya is swept downwind, where it consolidates against the receding edge of the polynya. The open water surface of the polynya is then once again exposed, fostering large heat losses. Dynamic polynya models based on this idea, for example, that of *Pease* [1987], are simple and easy to implement. However, the "real world" situation is far from being this simple. It was even noted by *Pease* [1987] that, in reality, as was observed at the Ronne Polynya, at low temperatures the frazil ice quickly consolidates into young ice floes with holes. Thus, under these conditions, the surface of a polynya is mostly covered with thin ice. In practice, polynyas are therefore often identified as areas of low sea ice concentration [*Morales Maqueda et al.*, 2004] and a number of studies designate the "open-water area" of a polynya as, e.g., sea ice of <14% [*Zwally et al.*, 1985] or ice of thickness <0.3 m [*Lynch et al.*, 1997].

[83] The presence of thin ice limits the magnitude of the surface turbulent heat losses compared to those over open water. It is therefore vital to be able to distinguish between open water and thin ice within a polynya in order to correctly model the surface sensible heat flux. The sensible heat flux is the largest component of the wintertime energy budget, when ice formation rates are greatest, and thus, the impact on dense water formation is at its largest. Therefore errors in the modeled sensible heat flux will lead to significant errors in the estimation of the impact of polynyas on dense water production volumes.

[84] In an investigation of ice production and associated dense water formation at coastal polynyas in the Antarctic, *Tamura et al.* [2008] assumed only the relatively narrow first regime of the Ronne Polynya to be of importance. This is indicated by their Figure 1, which corresponds to the first regime shown on Figure 4 of this paper. They concluded that the Ronne Polynya was therefore not responsible for the production of a large amount of ice or dense water. As indicated by their Figure 1, they did not include estimates of ice production rates in the region described herein as the second regime, as the production rates were assumed to be much smaller here than for the thinner ice of the first regime. The observations at the Ronne Polynya suggest this may not always be the case, as the heat flux over the second, thicker regime of the Ronne Polynya was found to be larger than might be expected, as a result of the perforations within the ice cover. This indicates the potential importance of the inclusion of ice concentration, as well as ice thickness, in the definition of a polynya area and illustrates the importance of in situ observations to the investigation of these processes.

[85] In conclusion, in order to accurately determine the effect of coastal polynyas on regional climate, sea ice formation, and accompanying dense water production rates, future research must include accurate parameterizations of the surface sensible heat flux appropriate to the surface conditions in order to correctly determine the wintertime

surface energy budget. In this way, the impact of coastal polynyas on the regional meteorology and oceanography of the high latitudes and on the global ocean circulation can be determined.

[86] **Acknowledgments.** This research was funded by a NERC studentship with CASE funding from the British Antarctic Survey. The authors would like to thank the operations staff at Rothera, as well as the pilots and the Air Unit. Russ Ladkin and Alex Weiss are also acknowledged for their contributions to this work, as well as Keith Nicholls, for his role as Ph.D. cosupervisor. The helpful comments of two anonymous reviewers are also gratefully acknowledged.

References

Alam, A., and J. A. Curry (1995), Lead-induced atmospheric circulations, *J. Geophys. Res.*, *100*(C3), 4643–4651, doi:10.1029/94JC02562.

Andreas, E. L., and B. A. Cash (1999), Convective heat transfer over wintertime leads and polynyas, *J. Geophys. Res.*, *104*(C11), 25,721–25,734, doi:10.1029/1999JC900241.

Andreas, E. L., and B. Murphy (1986), Bulk transfer coefficients for heat and momentum over leads and polynyas, *J. Phys. Oceanogr.*, *108*, 1875–1883.

Bannehr, L., and V. Glover (1991), Preprocessing of airborne pyranometer data, *Tech. Rep. NCAR/TN-364+STR*, National Center for Atmospheric Research, Boulder, Colo.

Brümmer, B. (1997), Boundary layer mass, water and heat budgets in wintertime cold-air outbreaks from the Arctic sea ice, *Mon. Weather Rev.*, *125*, 1824–1837.

Brümmer, B., D. Schröder, J. Launiainen, T. Vihma, A.-S. Smedman, and M. Magnusson (2002), Temporal and spatial variability of surface fluxes over the ice edge zone in the northern Baltic Sea, *J. Geophys. Res.*, *107*(C8), 3096, doi:10.1029/2001JC000884.

Busch, N. (1973), On the mechanics of atmospheric turbulence, in *Workshop on Micrometeorology*, edited by D. Haugen, pp. 1–65, Am. Meteorol. Soc., Boston, Mass.

Chang, S. S., and R. R. Braham (1991), Observational study of a convective internal boundary layer over Lake Michigan, *J. Atmos. Sci.*, *48*, 2265–2279.

Chapman, D. C. (1999), Dense water formation beneath a time-dependent coastal polynya, *J. Phys. Oceanogr.*, *29*, 807–820.

Chou, S.-H., and J. Zimmerman (1989), Bivariate conditional sampling of buoyancy flux during an intense cold air outbreak, *Boundary Layer Meteorol.*, *46*, 93–112.

Comiso, J. C., and A. L. Gordon (1998), Interannual variability in summer sea ice minimum, coastal polynyas and bottom water formation in the Weddell Sea, in *Antarctic Sea Ice: Physical Processes, Interaction, and Variability*, vol. 74, *Antarctic Res. Ser.*, edited by M. O. Jeffries, pp. 293–315, AGU, Washington, D. C.

Crawford, T., R. Dobosy, and E. Dumas (1996), Aircraft wind measurement considering lift-induced upwash, *Boundary Layer Meteorol.*, *80*, 79–94.

Dare, R. A., and B. W. Atkinson (1999), Numerical modeling of atmospheric response to polynyas in the southern sea ice zone, *J. Geophys. Res.*, *104*(D14), 16,691–16,708, doi:10.1029/1999JD900137.

DeCosmo, J., K. B. Katsaros, S. D. Smith, R. J. Anderson, W. A. Oost, K. Bumke, and H. Chadwick (1996), Air-sea exchange of water vapor and sensible heat: The Humidity Exchange Over the Sea (HEXOS) results, *J. Geophys. Res.*, *101*(C5), 12,001–12,016, doi:10.1029/95JC03796.

Donelan, M. A. (1990), Air-sea interaction, in *The Sea*, vol. 9, *Ocean Engineering Science*, edited by B. LeMehaute and D. M. Hanes, pp. 239–292, Wiley-Interscience, Hoboken, N. J.

Drennan, W. M., J. Zhang, J. R. French, C. McCormick, and P. Black (2007), Turbulent fluxes in the hurricane boundary layer. Part II: Latent heat flux, *J. Atmos. Sci.*, *64*, 1103–1115.

Fiedler, E. K. (2009), Air–sea-ice interactions at the Ronne Polynya, southern Weddell Sea, Antarctica, Ph.D. thesis, Univ. of East Anglia, Norwich, UK.

French, J. R., W. Drennan, J. Zhang, and P. Black (2007), Turbulent fluxes in the hurricane boundary layer: Part I. Momentum flux, *J. Atmos. Sci.*, *64*, 1089–1102.

Friehe, C., W. Shaw, D. Rogers, K. Davidson, W. Large, S. A. Stage, G. Crescenti, J. Khalsa, G. Greenhut, and F. Li (1991), Air-sea fluxes and surface layer turbulence around a sea surface temperature front, *J. Geophys. Res.*, *96*(C5), 8593–8609, doi:10.1029/90JC02062.

Gallée, H. (1997), Air-sea interactions over Terra Nova Bay during winter: Simulation with a coupled atmosphere-polynya model, *J. Geophys. Res.*, *102*(D12), 13,835–13,849, doi:10.1029/96JD03098.

Garman, K., K. Hill, P. Wyss, M. Carlsen, J. Zimmerman, B. Stirm, T. Carney, R. Santini, and P. Shepson (2006), An airborne and wind tunnel evaluation of a wind turbulence measurement system for aircraft-based flux measurements, *J. Atmos. Oceanic. Technol.*, *23*, 1696–1708.

Garratt, J. R. (1990), The internal boundary layer - a review, *Boundary Layer Meteorol.*, *50*, 171–203.

Grossman, R. L., and A. K. Betts (1990), Air-sea interaction during an extreme cold air outbreak from the eastern coast of the United States, *Mon. Weather Rev.*, *118*, 324–342.

Hartmann, D. L. (1994), *Global Physical Climatology*, vol. 56, *Int. Geophys. Ser.*, 408 pp., Academic, London.

Hartmann, J., C. Kottmeier, C. Wamser, and E. Augstein (1994), Aircraft measured atmospheric momentum, heat and radiation fluxes over Arctic sea ice, in *The Polar Oceans and Their Role in Shaping the Global Environment*, *Geophys. Monogr. Ser.*, vol. 85, edited by O. M. Johannessen, R. D. Muench, and J. E. Overland, pp. 443–454, AGU, Washington, D. C.

Kottmeier, C., and D. Engelbart (1992), Generation and atmospheric heat-exchange of coastal polynyas in the Weddell Sea, *Boundary Layer Meteorol.*, *60*, 207–234.

Lenschow, D. H. (1986), Aircraft measurements in the boundary layer, in *Probing the Atmospheric Boundary Layer*, edited by D. H. Lenschow, pp. 39–55, Am. Meteorol. Soc., Boston, Mass.

Liu, A., S. Martin, and R. Kwok (1997), Tracking of ice edges and ice floes by wavelet analysis of SAR images, *J. Atmos. Oceanic Technol.*, *14*(5), 1187–1198.

Lynch, A. H., M. F. Glueck, W. L. Chapman, D. A. Bailey, and J. E. Walsh (1997), Satellite observation and climate system model simulation of the St. Lawrence Island polynya, *Tellus*, *49A*, 277–297.

Markus, T., C. Kottmeier, and E. Fahrbach (1998), Ice formation in coastal polynyas in the Weddell Sea and their impact on oceanic salinity, in *Antarctic Sea Ice: Physical Processes, Interaction, and Variability*, vol. 74, *Antarctic Res. Ser.*, edited by M. O. Jeffries, pp. 273–292, AGU, Washington, D. C.

Melfi, S. H., J. D. Spinhirne, S.-H. Chou, and S. P. Palm (1985), Lidar observations of vertically organized convection in the planetary boundary layer over the ocean, *J. Clim. Appl. Meteorol.*, *24*, 806–821.

Morales Maqueda, M. A., A. J. Willmott, and N. R. T. Biggs (2004), Polynya dynamics: A review of observations and modeling, *Rev. Geophys.*, *42*, RG1004, doi:10.1029/2002RG000116.

Nicholls, K. W., L. Padman, M. Schröder, R. A. Woodgate, A. Jenkins, and S. Østerhus (2003), Water mass modification over the continental shelf north of Ronne Ice Shelf, Antarctica, *J. Geophys. Res.*, *108*(C8), 3260, doi:10.1029/2002JC001713.

Nicholls, K. W., K. Makinson, and S. Østerhus (2004), Circulation and water masses beneath the northern Ronne Ice Shelf, Antarctica, *J. Geophys. Res.*, *109*, C12017, doi:10.1029/2004JC002302.

Paulson, C. (1970), The mathematical representation of wind speed and temperature profiles in the unstable atmospheric surface layer, *J. Appl. Meteorol.*, *9*, 857–861.

Pease, C. H. (1987), The size of wind-driven coastal polynyas, *J. Geophys. Res.*, *92*(C7), 7049–7059, doi:10.1029/JC092iC07p07049.

Petersen, G. N., and I. A. Renfrew (2009), Aircraft-based observations of air-sea fluxes over Denmark Strait and the Irminger Sea during high wind speed conditions, *Q. J. R. Meteorol. Soc.*, *135*, 2030–2045.

Pinto, J. O., and J. A. Curry (1995), Atmospheric convective plumes emanating from leads 2. Microphysical and radiative processes, *J. Geophys. Res.*, *100*(C3), 4633–4642, doi:10.1029/94JC02655.

Pinto, J. O., J. A. Curry, and K. L. McInnes (1995), Atmospheric convective plumes emanating from leads. 1. Thermodynamic structure, *J. Geophys. Res.*, *100*(C3), 4621–4631, doi:10.1029/94JC02654.

Renfrew, I. A., and J. C. King (2000), A simple model of the convective internal boundary layer and its application to surface heat flux estimates within polynyas, *Boundary Layer Meteorol.*, *94*, 335–356.

Renfrew, I. A., J. C. King, and T. Markus (2002), Coastal polynyas in the southern Weddell Sea: Variability of the surface energy budget, *J. Geophys. Res.*, *107*(C6), 3063, doi:10.1029/2000JC000720.

Schauer, U., and E. Fahrbach (1999), A dense bottom water plume in the western Barents Sea: Downstream modification and interannual variability, *Deep Sea Res., Part I*, *46*, 2095–2108.

Schröder, D., T. Vihma, A. Kerber, and B. Brümmer (2003), On the parameterization of turbulent surface fluxes over heterogeneous sea ice surfaces, *J. Geophys. Res.*, *108*(C6), 3195, doi:10.1029/2002JC001385.

Smith, S. D. (1988), Coefficients for sea surface wind stress, heat flux, and wind profiles as a function of wind speed and temperature, *J. Geophys. Res.*, *93*(C12), 15,467–15,472, doi:10.1029/JC093iC12p15467.

Smith, S. D., R. D. Muench, and C. H. Pease (1990), Polynyas and leads: An overview of physical processes and environment, *J. Geophys. Res.*, *95*(C6), 9461–9479, doi:10.1029/JC095iC06p09461.

Spreen, G., L. Kaleschke, and G. Heygster (2008), Sea ice remote sensing using AMSR-E 89 GHz channels, *J. Geophys. Res.*, *113*, C02S03, doi:10.1029/2005JC003384.

Stull, R. (1988), *An Introduction to Boundary Layer Meteorology*, 666 pp., Kluwer Acad., Dordrecht, Netherlands.

Tamura, T., K. I. Ohshima, and S. Nihashi (2008), Mapping of sea ice production for Antarctic coastal polynyas, *Geophys. Res. Lett.*, *35*, L07606, doi:10.1029/2007GL032903.

Walkington, I. A., and A. J. Willmott (2006), A coupled coastal polynya-atmospheric boundary layer model, *J. Phys. Oceanogr.*, *36*, 897–914.

Walter, B. A. (1989), A study of the planetary boundary layer over the polynya downwind of St. Lawrence Island in the Bering Sea using aircraft data, *Boundary Layer Meteorol.*, *48*, 255–282.

Walter, B. A., D. J. Cavalieri, K. Thornhill, and A. Gasiewski (2006), Aircraft measurements of heat fluxes over wind-driven coastal polynyas in the Bering Sea, *IEEE Trans. Geosci. Remote Sens.*, *44*(11), 3118–3134.

Winsor, P., and G. Björk (2000), Polynya activity in the Arctic Ocean, 1958–1997, *J. Geophys. Res.*, *105*(C4), 8789–8803, doi:10.1029/1999JC900305.

Zwally, H. J., J. C. Comiso, and A. L. Gordon (1985), Antarctic offshore leads and polynyas and oceanographic effects, in *Oceanology of the Antarctic Continental Shelf*, vol. 43, *Antarctic Res. Ser.*, pp. 203–226, AGU, Washington, D. C.

E. K. Fiedler, Met Office, Exeter, EX1 3PB UK. (emma.fiedler@metoffice.gov.uk)

J. C. King and T. A. Lachlan-Cope, British Antarctic Survey, Cambridge, UK.

I. A. Renfrew, School of Environmental Sciences, University of East Anglia, Norwich, UK.